
Oral presentation | Multi-phase flow

Multi-phase flow-IV

Tue. Jul 16, 2024 10:45 AM - 12:45 PM Room D

[4-D-04] When does a drop stop bouncing on a cold surface?

*Mingguang she Shen¹, Ben Q Li² (1. Yancheng Teachers University, 2. University of Michigan-Dearborn)

Keywords: Phase field, Drop bouncing, Two-phase flow

When does a drop stop bouncing on a cold surface?

Mingguang Shen^a, Ben Q. Li^{b,*}

^a *School of Mathematics and Statistics, Yancheng Teachers University, Yancheng, 224002, PR China*

^b *Department of Mechanical Engineering, University of Michigan, Dearborn, MI 48128, USA*

Abstract

Drop bouncing is intriguing when interacting with solidification. However, the interaction between drop bouncing and solidification is less known. This paper delves into drop bouncing in practical three dimensional printing conditions. A phase field model coupled with the enthalpy porosity model was employed to capture the evolving liquid-gas and liquid-solid interfaces. The model was discretized using a finite difference method on a half-staggered grid and was run in a parallel fashion. The parameters influencing drop bouncing were investigated. They include impact velocity, drop size and surface wettability. Moreover, a theoretical model based on energy analysis was put forward to predict drop bouncing on cold surfaces. The major findings are as follows. For a fixed undercooling, increasing impact velocity or reducing contact angle will significantly reduce drop bouncing, while increasing drop size does little to mitigate bouncing. The theoretical model suggests that for a fixed undercooling, bouncing is avoided if the maximum spread is large enough. The smaller the drop size, the larger the maximum spread.

Key words: Phase field; Drop bouncing; Normal impact; Two-phase flow.

* Corresponding author.

Email address: benqli@umich.edu (B.Q. Li).

Telephone number: 001 (313)593-5241 (B.Q. Li).

1. Introduction

Drop bouncing on a solid surface is an interesting natural and industrial phenomenon [1-3]. If a rain drop hit the windshield of a car, the drop would probably bounce off, or slide along the windshield, leaving a trace of water affecting the eyesight of the driver. Drop bouncing in this case is thus beneficial. However, in other situations such as three dimensional printing and thermal spraying, drop bouncing is to be avoided. For instance, in thermal spraying, regular splats or disk-like splats are desired [4]. This type of splats is formed by the fast spreading and the subsequent rapid solidification. Therefore, it is of significance to delve into the interaction between solidification and bouncing in drop impact in related industries.

Drop bouncing may occur during drop retracting, which directly follows drop spreading. Drop bouncing is a possible outcome of drop impact, which is the competition among several factors, such as inertial force, surface tension, viscous force, drop size, impact velocity, and so on [5]. Two dimensionless numbers can be employed to embody the abovementioned factors. One is the Reynolds (Re) number and the other is the Weber (We) number. They are defined as follows [6].

$$Re = \frac{\rho l v}{\mu}, We = \frac{\rho v^2 l}{\gamma} \quad (0)$$

where ρ represents the density of a drop, l is a characteristic length, v is impact velocity, μ is the viscosity of the drop, and γ is the surface tension coefficient between the drop and the surrounding medium. The Re number measures the relative importance between inertia and viscous forces, and the We number measures that between inertia and surface tension.

Drop bouncing has been studied extensively in experiments and numerical simulations in a wide range of the We and Re numbers. In experiments, drop size concentrates mostly on millimeters, and impact velocity on 1~10 m/s [7]. Compared with numerical simulations, experimental works cannot access to a wide range of impact velocities and capture instantaneous drop profiles.

Wang et al. [8] experimentally studied drop bouncing isothermally off an incline for $We < 70$, finding that the contact time is reduced due to asymmetric spreading. Increasing impact velocity or inclination angles both help facilitate early detachment. In this oblique impact, the characteristic velocity was chosen as the projection of impact velocity onto the direction perpendicular to the incline. Samkhaniani et al. [9], using a phase field method, examined the bouncing dynamics of a drop hitting onto a superhydrophobic surface. The cases under consideration have $We < 60$. Besides, they proposed a new model for the contact time. Sanjay et al. [10] investigated the transition between bouncing and deposition for an impacting drop of $We \sim 50$ onto a solid surface, and gave a theoretical correlation for the transition. They did not however consider heat transfer in the impact processes.

To the best knowledge of the authors, there are few studies examining the transition between bouncing and deposition in drop impact with phase change. This paper developed a phase field model to that end. This paper also investigated the effects of impact velocity, contact angle and drop size on drop bouncing. Moreover, a theoretical model to predict the transition between bouncing and deposition was proposed based on the model of Sanjay et al. [10].

2. Governing equations

2.1 Cahn-Hilliard equation

Consider two-phase flows of incompressible Newtonian fluids. The governing equations consist of an equation to track the fluid-fluid interface, the continuity equation, the Navier-Stokes equation, and the heat balance equation. The phase field equation is employed to track the interface and is introduced first [11].

$$\frac{DC}{Dt} = \nabla \cdot (M \nabla \varphi) \quad (1)$$

Eq. (1) is the advective Cahn-Hilliard equation, with M being the phase field mobility and C being the phase field. $D()/Dt$ is the material derivative and t is time. Herein $C=1$ denotes a liquid and $C=-1$ a gas. The interface spans where $-1 < C < 1$, as shown in Fig. 1(b).

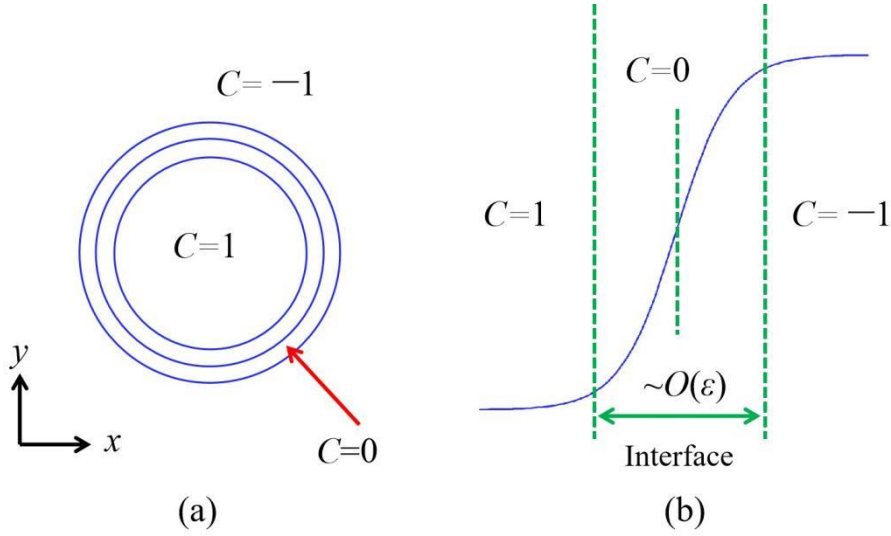


Fig. 1. Phase field distribution. (a) displays a droplet with a diffuse interface. (b) gives a magnified view of the interface. The interface has a thickness of order ε .

φ on the right-hand side of Eq. (1) is the chemical potential, defined as below in Eq. (2) [11].

$$\varphi = \frac{\lambda}{\varepsilon^2} C(C^2 - 1) - \lambda \Delta C \quad (2)$$

$$\lambda = \frac{3\sqrt{2}}{4} \gamma \varepsilon \quad (3)$$

where λ is the mixing free energy density and ε is the characteristic interface thickness.

Δ is the Laplacian operator. γ in Eq. (3) is the surface tension coefficient.

2.2 Flow field equations

The fluid field equations contain the mass conservation equation, the momentum conservation equation, and the heat balance equation [12].

$$\nabla \cdot \mathbf{u} = 0 \quad (4)$$

$$\rho \frac{D\mathbf{u}}{Dt} = -\nabla p + \nabla \cdot \boldsymbol{\sigma} + \rho \mathbf{g} + \varphi \nabla C + \mathbf{S} \quad (5)$$

$$\rho c_P \frac{DT}{Dt} = \nabla \cdot (k \nabla T) - \rho_l L_l \frac{\partial \eta}{\partial t} \quad (6)$$

In the equations above, ρ is density, \mathbf{u} is velocity, p is pressure, $\boldsymbol{\sigma} = \mu[\nabla \mathbf{u} + (\nabla \mathbf{u})^T]$ is the Newtonian stress tensor. \mathbf{g} is the gravitational acceleration. Surface tension is converted as $\varphi \nabla C$. c_P is the heat capacity at constant pressures, k is thermal conductivity, and L_l is the latent heat of fusion of the liquid. \mathbf{S} is a momentum sink, taking on the following form that assumes porous media flows near a solidifying front [12].

$$\mathbf{S} = -d \frac{(1 - \eta)^2}{\eta^3 + b} \mathbf{u} \quad (7)$$

d is the mushy zone constant and $b=0.001$. The porosity is denoted with the liquid fraction η , as in Eq. (8) where T_m is the melting point of the liquid and ΔT is a small temperature interval [12].

$$\eta = \begin{cases} 1 & T > T_m + \Delta T \\ \frac{T - (T_m - \Delta T)}{2\Delta T} & T_m - \Delta T \leq T \leq T_m + \Delta T \\ 0 & T < T_m - \Delta T \end{cases} \quad (8)$$

Moreover, as a diffuse interface approach is adopted in this paper, field parameters are formulated as functions of the phase field C , for instance

$$\rho = \frac{1 - C}{2} \rho_g + \frac{1 + C}{2} \rho_l \quad (9)$$

with the subscripts g and l representing gas and liquid, respectively.

2.3 Boundary conditions & Numerical procedures

Boundary conditions and numerical procedures have been elaborated on in detail in [12]. Only the setup of the contact angle θ is introduced here. The contact angle θ is defined as the angle the triple phase line makes with a substrate, as shown in Fig. 2.

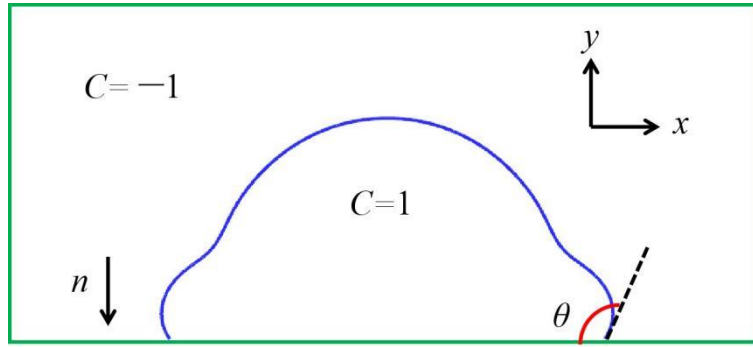


Fig. 2. Definition of the contact angle θ .

In this paper, the contact angle is fixed throughout the contact line motion. In other words, a static contact angle model is employed here, taking on the form as in Eq. (10) [13].

$$\frac{\partial C}{\partial n} = \frac{\sqrt{2} \cos \theta}{2 \varepsilon} (1 - C^2) \quad (10)$$

where n is the coordinate perpendicular to the boundary and pointing into the substrate, as shown in Fig. 2.

3. Results and discussion

3.1 Validation of the model

3.1.1 Isothermal impact

Fig. 3 gives the comparison of drop profiles about a molten Tin drop impinging, isothermally, onto a solid surface. The drop has a diameter of 2.7 mm and an impact speed of 1 m/s. The drop is in point contact with the substrate at the beginning. $\theta=140^\circ$ and $\Delta x=50 \mu\text{m}$. The number of total grid points is $66 \times 111 \times 66$ and the time step Δt is 1 μs . Moreover, $\varepsilon=100 \mu\text{m}$ and $M=1 \times 10^{-9} \text{m}^3 \cdot \text{s} \cdot \text{kg}^{-1}$. For material properties, the reader could consult [12]. The experiment was conducted by Aziz et al. [14]. The simulation was done in [12], but with a phase field model with a different free energy density. In that work, the phase field took on the values of 1 and 0.

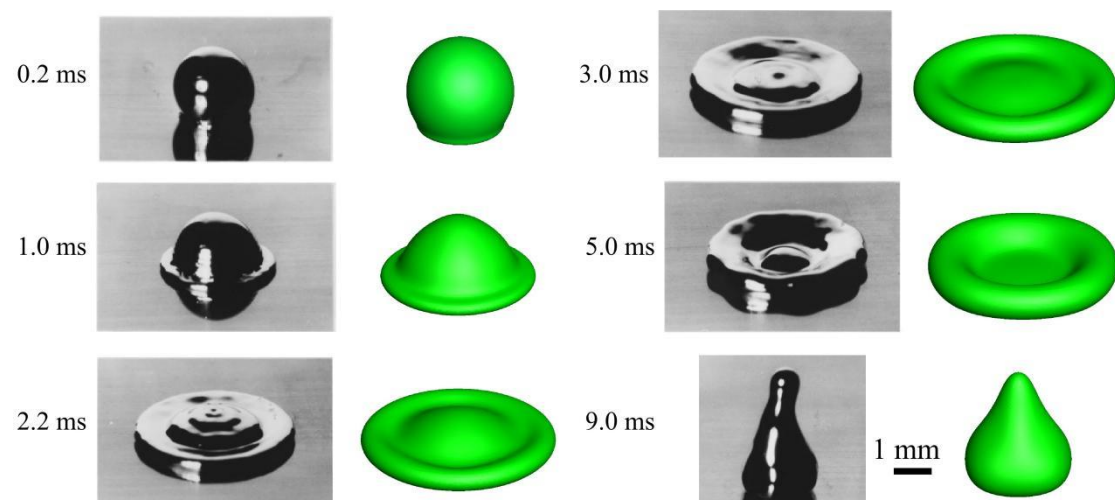


Fig. 3. Comparison of drop profiles for the Tin drop impact ($v=1 \text{ m/s}$). The scale bar is only for the numerical outcome. The experiment was conducted by Aziz et al. [14]. The simulation was done in [12] using another phase field model with a different free energy density.

As can be found in Fig. 3, the comparison is reasonably good. Since the interface should be adequately resolved by the grid, ε is made to equal $2\Delta x$ so that the diffuse interface is resolved by about 8 points. Moreover, there are 54 cells across the drop diameter (D). The Cahn (Cn) number is used to denote grid fineness [15]

$$Cn = \frac{\varepsilon}{D} = \frac{2\Delta x}{54\Delta x} = \frac{1}{27} \quad (11)$$

This value has been demonstrated small enough to ensure grid independence.

3.1.2 Non-isothermal impact

The other validation case is about a Tin drop impact onto a cold surface. The drop has a diameter of 2.7 mm and an impact speed of 1 m/s. The drop is in point contact with the substrate at the beginning. $\theta=140^\circ$ and $\Delta x=50 \mu\text{m}$. The number of total grid points is $66 \times 111 \times 66$ and the time step Δt is $0.5 \mu\text{s}$. Moreover, $\varepsilon=100 \mu\text{m}$ and $M=1 \times 10^{-9} \text{m}^3 \cdot \text{s} \cdot \text{kg}^{-1}$. The thermal contact resistance is tuned to $R''=1 \times 10^{-5} \text{m}^2 \cdot \text{K} / \text{W}$. Initially the drop and the surrounding gas are at 513 K, and the substrate is at 298 K. The numerical outcome is presented in Fig. 4.

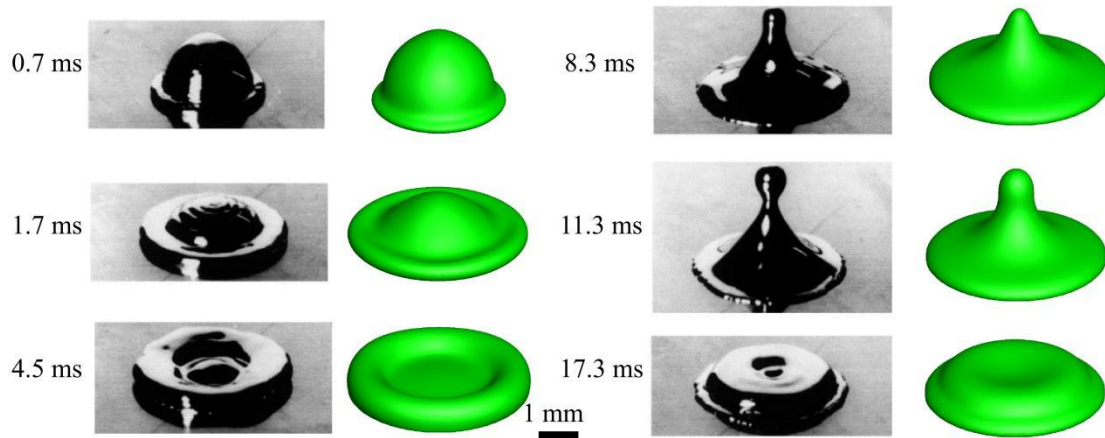


Fig. 4. Comparison of drop profiles for the Tin drop impact undergoing solidification ($v=1 \text{ m/s}$). The scale bar is only for the numerical outcome. The experiment was by Aziz et al. [14]. The simulation was done in [12] using another phase field model with a different free energy density.

Overall, the numerical outcome is consistent with the experiment, though some tiny features are not captured. When the drop flattens to the maximum, recoiling follows. However, as the bottom of the drop has been frozen, the remaining liquid flows back on the newly solidified Tin, converging at the impact center and then rising into the air, as shown at 11.3 ms.

3.2 Bouncing inhibition mechanisms

As can be seen in Fig. 4 in the last section, there is a finger rising into the air at 11.3 ms. The finger is driven by the back flow induced by surface tension. Now comes the question: how to eliminate the finger? One possible way is to render more liquid in contact with the substrate solidified so that the remaining is not able to rise even if surface tension is strong enough. To render more liquid frozen, there may exist a couple of ways, like increasing contact area. Guided by this philosophy, we investigated the effects of impact velocity, drop radius, and contact angle, respectively.

3.2.1 Increasing impact velocity

In this section, impact velocity varies. The drop has a diameter of 2.7 mm and is in point contact with the substrate at the beginning. $\theta=120^\circ$ and $\Delta x=50\ \mu\text{m}$. The number of total grid points is $101\times 71\times 101$ and the time step Δt is $0.25\ \mu\text{s}$. Moreover, $\varepsilon=100\ \mu\text{m}$ and $M=4\times 10^{-9}\ \text{m}^3\cdot\text{s}\cdot\text{kg}^{-1}$. The thermal contact resistance is tuned to $R''=1\times 10^{-5}\ \text{m}^2\cdot\text{K}/\text{W}$. Initially the drop and the surrounding gas are at 513 K, and the substrate is at 298 K. Impact velocity increases evenly from 1 m/s to 2 m/s, with an increment of 0.5 m/s. The numerical outcome is presented below in Fig. 5.

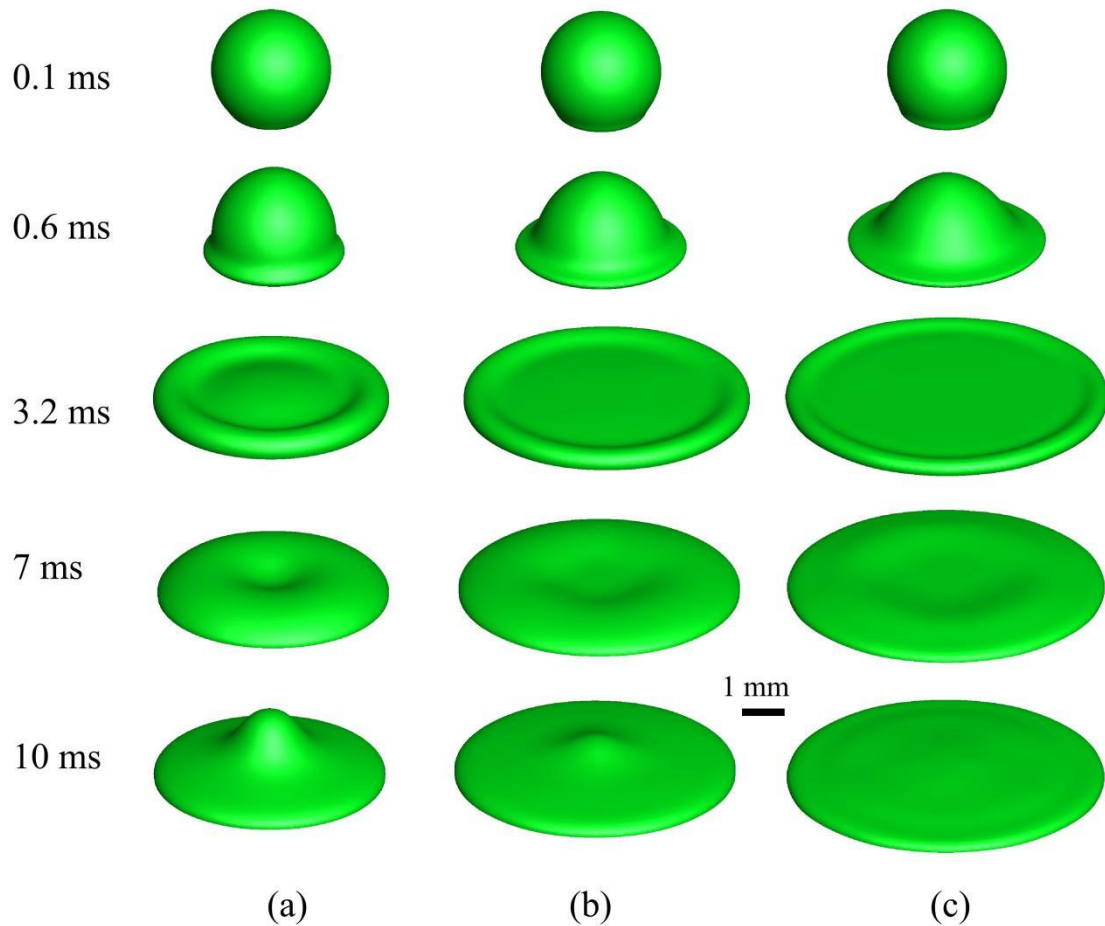


Fig. 5. Morphology change of a Tin drop with varied impact velocities. The drop radius is 1.35 mm and the contact angle is 120° . Impact velocity is 1 m/s in (a), 1.5 m/s in (b), and 2 m/s in (c), respectively.

As expected, when the impact velocity is increased, the drop morphology changes dramatically as time goes on. There is an evident finger lifting at 10 ms when the impact velocity is 1 m/s, while none of this kind occurs for velocities at and beyond 1.5 m/s. Since more liquid in contact with the substrate is frozen, less liquid could be driven by surface tension to form a finger. The final drop profile resembles a pancake, which is regular and desired.

3.2.2 Increasing drop radius

This section is to examine the role of drop radius in eliminating finger liftings. Drop radius is varied in this section. The drop is in point contact with the substrate at the beginning, and impact velocity is 1 m/s. $\theta=140^\circ$ and $\Delta x=50 \mu\text{m}$. The number of total grid points is $101 \times 71 \times 101$ and the time step Δt is $0.25 \mu\text{s}$. Moreover, $\varepsilon=100 \mu\text{m}$ and $M=4 \times 10^{-9} \text{ m}^3 \cdot \text{s} \cdot \text{kg}^{-1}$. The thermal contact resistance is tuned to $R''=1 \times 10^{-5} \text{ m}^2 \cdot \text{K}/\text{W}$. Initially the drop and the surrounding gas are at 513 K, and the substrate is at 298 K. The drop radius increases evenly from 1 mm to 1.7 mm, with an increment of 0.35 mm. The numerical outcome is shown in Fig. 6.

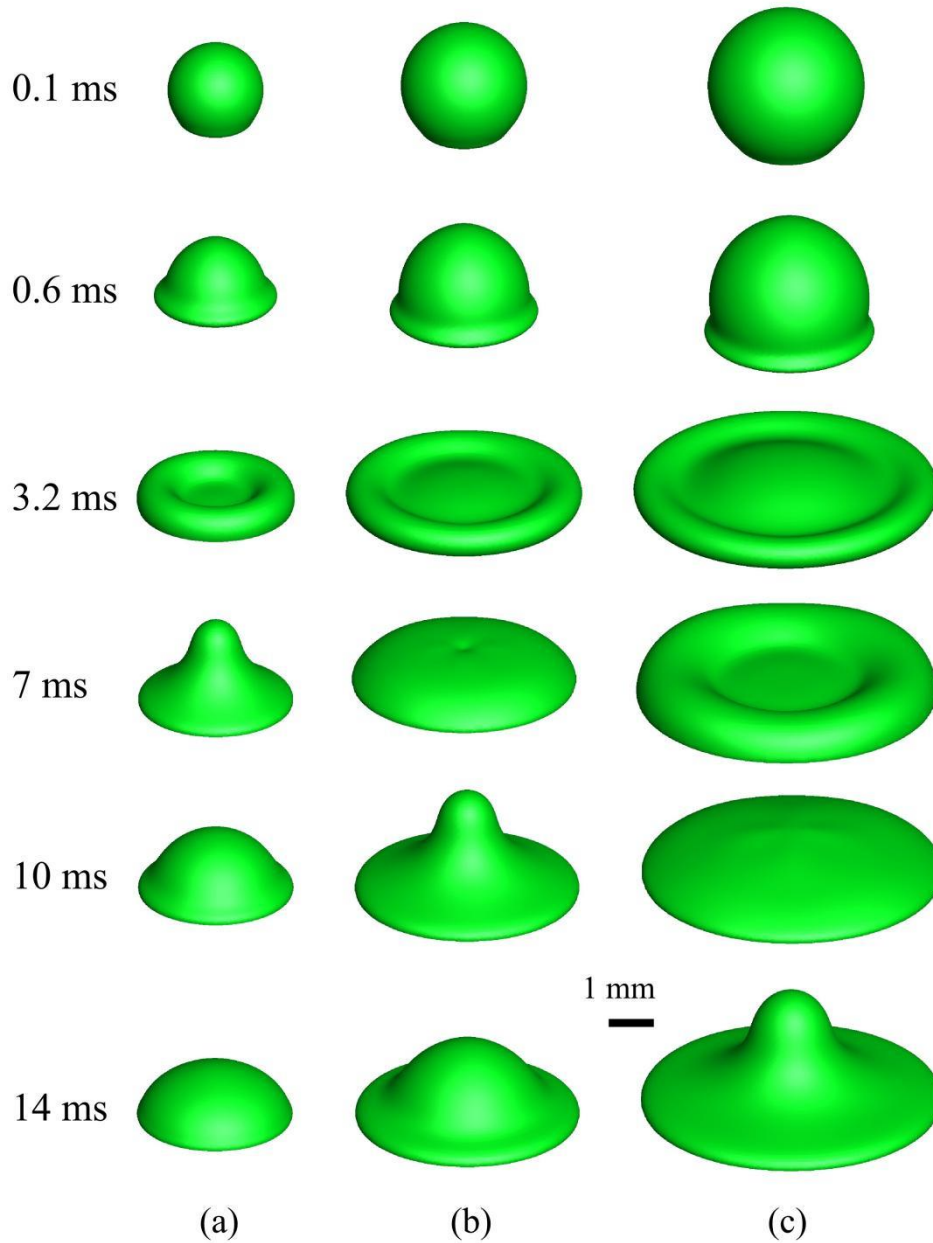


Fig. 6. Morphology change of a Tin drop with varied drop radii. Impact velocity is 1 m/s and the contact angle is 140° . The drop radius is 1 mm in (a), 1.35 mm in (b), and 1.7 mm in (c), respectively.

As demonstrated herein, varying drop radius does not help hinder finger liftings.

When drop radius is reduced to 1 mm, bouncing occurs earlier than it does in the case of radius 1.35 mm. However, when drop radius is increased to 1.7 mm, there is no finger lifting before 10 ms. Nevertheless, it is clear that a finger lifting will appear afterwards, since there is a clear back flow as demonstrated in the narrowing of the central film at 10 ms.

3.2.3 Reducing contact angle

This section is to examine the role of contact angle in eliminating finger liftings. Contact angle is varied in this section. The drop has a diameter of 2.7 mm and is in point contact with the substrate at the beginning. Impact velocity is 1 m/s and $\Delta x=50 \mu\text{m}$. The number of total grid points is $101 \times 71 \times 101$ and the time step Δt is $0.25 \mu\text{s}$. Moreover, $\varepsilon=100 \mu\text{m}$ and $M=4 \times 10^{-9} \text{m}^3 \cdot \text{s} \cdot \text{kg}^{-1}$. The thermal contact resistance is tuned to $R''=1 \times 10^{-5} \text{m}^2 \cdot \text{K} / \text{W}$. Initially the drop and the surrounding gas are at 513 K, and the substrate is at 298 K. The contact angle decreases evenly from 140° to 60° , with an increment of 40° . The numerical outcome is shown in Fig. 7.

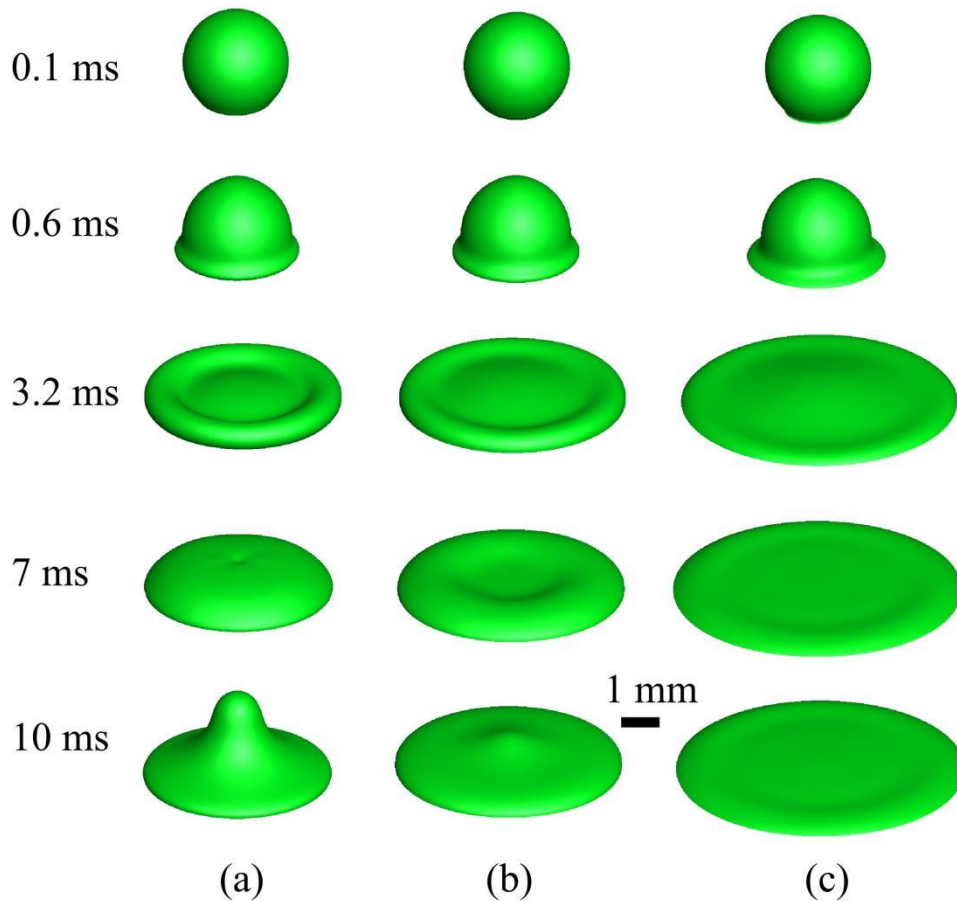


Fig. 7. Morphology change of a Tin drop with varied contact angles. The drop radius is 1.35 mm and impact velocity is 1 m/s. The contact angle is 140° in (a), 100° in (b), and 60° in (c), respectively.

Fig. 7 shows that reducing contact angle actually helps hinder finger liftings. In

the cases under consideration, the finger lifting appears to be completely eliminated when contact angle is smaller than 100° . The reason behind the suppression of finger liftings is the same as in increasing impact velocity. Smaller contact angles mean larger contact area between the drop and the substrate, and hence shortened solidification time.

3.3 Bouncing&deposition transition

In this section, a theoretical model was established to give a quantitative description on the transition from deposition to bouncing. A schematic of drop bouncing on a cold surface is given below in Fig. 8 where the green represents the newly solidified portion with height h and the blue the iso-contour of $C=0$. The flow denoted by red is incurred by surface tension. Moreover, solidification is assumed to commence mainly after the drop reaches the maximum spread.

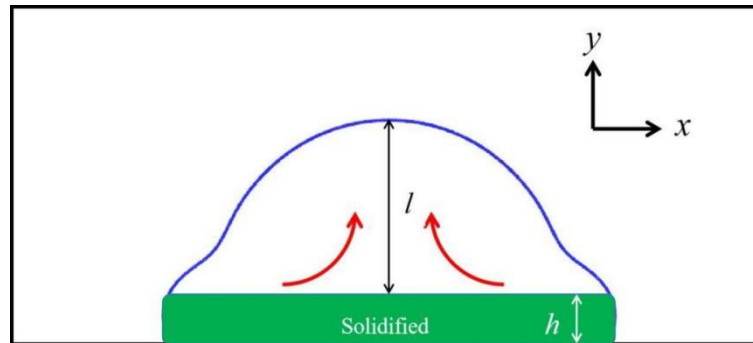


Fig. 8. Schematic of a bouncing drop on a cold surface. h is the solidification thickness and l is the rising height. The red arrows signifies the back flow induced by surface tension.

Two dimensionless numbers can be defined to characterize the impact process.

One is the Bond (Bo) number and another is the (Oh) number [10].

$$Bo = \frac{\rho g l^2}{\gamma}, Oh = \frac{\mu}{\sqrt{\rho \gamma l}} \quad (12)$$

The Bond (Bo) number measures the relative importance of gravity and surface tension.

The relative importance of viscous force, inertia and capillary force is given by the

Ohnesorge (Oh) number. ρ and η represent liquid properties. l is a characteristic length scale, for instance drop diameter (D) or drop radius (R).

In this paper, emphasis is given to the cases with $Bo < 1$ and $Oh < 1$. If $Oh > 1$, the drop stops bouncing due to viscous dissipation [16]. If $Bo > 1$, gravity helps inhibit bouncing [17].

If the maximum spread comes not too large, scaling as R , then one can presume that prior to retraction, the surface energy of the drop scales as

$$E_s \sim \gamma R^2 \quad (13)$$

As the drop retracts, a boundary layer develops on the substrate, with the thickness scaling as R . Then the viscous dissipation during drop retraction scales as [18]

$$E_d \sim \eta \frac{V_r}{R} R^3 \quad (14)$$

where $V_r = (\gamma/\rho R)^{0.5}$ is the inertial-capillary velocity. If surface energy is just able to lift the drop off the substrate, meaning the rising height is on the order of the drop radius R , then gravitational potential energy scales as

$$E_g \sim \rho g R^4 \quad (15)$$

Assuming surface energy is totally converted into viscous dissipation and gravitational energy, one has

$$E_s \sim E_d + E_g \quad (16)$$

Dividing both sides of Eq. (16) by γR^2 would lead to a criterion for drops bouncing off a surface without phase change.

$$Oh + Bo \sim 1 \quad (17)$$

When solidification is on, surface energy E_s is converted into three kinds of energies, namely, viscous dissipation E_d , potential energy E_g , and the energy consumed in solidification E_c . The effect of solidification in restricting droplet retracting lies in the fact that all the kinetic energy stored in the solidified layer is lost.

$$E_c \sim h(\beta R)^2 \rho V_r^2 \quad (18)$$

β is the maximum flattening ratio, defined as the ratio of the maximum spread to the initial drop diameter/radius and h is the solidification thickness, which is related to the solidifying velocity V_i [19]

$$V_i = \frac{dh}{dt} = \frac{T_m - T_{sub}}{\frac{1}{\mu_i} + \rho L \left(\frac{h}{k} + \frac{1}{h_c} \right)} \quad (19)$$

T_m is the melting point of the drop, T_{sub} is the temperature of the substrate. μ_i is the interface kinetic coefficient, L is the latent heat of the drop, k is the thermal conductivity of the solidified portion, h_c is the interface heat transfer coefficient.

Rearrangement of Eq. (19) gives

$$\left[\frac{1}{\mu_i} + \rho L \left(\frac{h}{k} + \frac{1}{h_c} \right) \right] dh = (T_m - T_{sub}) dt \quad (20)$$

Integrating on both sides yields

$$\frac{\rho L h^2}{k} \frac{1}{2} + \left(\frac{1}{\mu_i} + \frac{\rho L}{h_c} \right) h = (T_m - T_{sub}) t + C_1 \quad (21)$$

Assume that $t=0$ corresponds to the instant when the drop starts to recoil and when solidification thickness h is approximately zero. Therefore,

$$C_1 = 0 \quad (22)$$

Now, consider the transition from bouncing to non-bouncing when solidification is on. The solidified thickness h , at the critical moment when the drop is lifted off, scales as,

$$\frac{\rho L h^2}{k} \frac{1}{2} + \left(\frac{1}{\mu_i} + \frac{\rho L}{h_c} \right) h \sim (T_m - T_{sub}) \frac{R}{V_r} \quad (23)$$

where the retracting time is approximately R/V_r . Further simplification yields

$$h \sim \frac{-\left(\frac{1}{\mu_i} + \frac{\rho L}{h_c} \right) + \sqrt{\left(\frac{1}{\mu_i} + \frac{\rho L}{h_c} \right)^2 + 2 \frac{\rho L}{k} (T_m - T_{sub}) \frac{R}{V_r}}}{\frac{\rho L}{k}} \quad (24)$$

Having estimated all the variables involved, one is in a position to derive a criterion. Balancing all the energies gives Eq. (25), with the assumption $l \sim R$.

$$\gamma R^2 \sim \eta \frac{V_r}{R} R^3 + \rho g R^4 + h (\beta R)^2 \rho V_r^2 \quad (25)$$

Dividing both sides by γR^2 , one would obtain a modified criterion for drops bouncing on cold surfaces.

$$Oh + Bo + We \sim 1 \quad (26)$$

where $We = h \beta^2 \rho V_r^2 / \gamma$. If h is large enough, solidification has to be taken into account. For instance, when $Oh + Bo \sim We$, one has $We \sim 0.5$. This would give a critical solidification thickness scaling as

$$h \sim 0.5 \frac{\gamma}{\rho \beta^2 V_r^2} \quad (27)$$

Combining Eq. (24) and Eq. (27), one would obtain a critical radius in a fixed impact

velocity, for a liquid drop impacting onto a specific substrate.

For the parameters under consideration, Eq. (24) can be further simplified as

$$h \sim \sqrt{\frac{k}{\rho L} (T_m - T_{sub})} \frac{R}{V_r} \quad (28)$$

Balancing Eq. (28) and Eq. (27) would lead to

$$\sqrt{\frac{k}{\rho L} (T_m - T_{sub})} \frac{R}{V_r} \sim \frac{\gamma}{\rho \beta^2 V_r^2} \quad (29)$$

Rearrangement yields

$$\beta_c \sim \gamma^{0.5} \left[(T_m - T_{sub}) \frac{k\gamma}{L} \right]^{-0.25} \left(\frac{\gamma}{\rho R} \right)^{-0.125} \quad (30)$$

Eq. (30) gives the smallest flattening ratio β_c that would not allow for bouncing after impact. β_c is graphed in Fig. 9 and the numerical outcomes conducted are inserted.

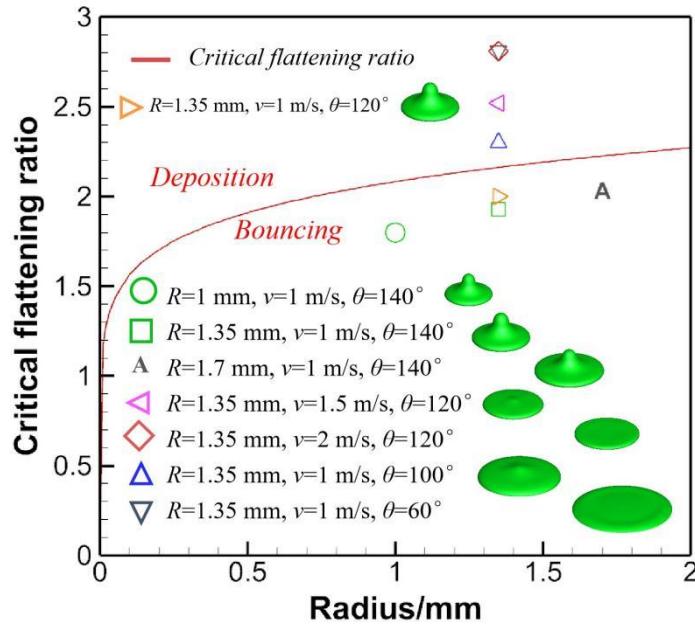


Fig. 9. Phase diagram of drop impact on a cold surface. The solid line is the graph of the critical flattening ratio, above which deposition dominates and below which bouncing dominates.

Fig. 9 shows that drop bouncing is predicted for those having a maximum flattening ratio smaller than the corresponding critical flattening ratio. For those to the

opposite, drop bouncing mitigation or elimination is observed as well.

4. Concluding remarks

To predict the transition between bouncing and deposition, a phase field model coupled with the enthalpy porosity model was developed to simulate drop impact onto a cold surface. The impacting parameters are in real three dimensional printing conditions. The major findings are as follows.

1) For a fixed undercooling, drop bouncing will be significantly mitigated when impact velocity is increased. This would lead to an augmented maximum spread, and hence more volume to be solidified. Thus less liquid is to be pulled up by surface tension.

2) For a fixed undercooling, increasing drop size will lead to an augmented maximum spread. But this will not help mitigate drop bouncing, since increasing drop size bring together more liquid, and hence more time to solidify. In this case, drop bouncing is delayed, rather than mitigated.

3) For a fixed undercooling, reducing contact angle will significantly reduce drop bouncing. The reason behind is the same as increasing impact velocity. That is, more liquid in contact with the solid surface will be frozen.

Further work could be done regarding drop bouncing on inclined cold surfaces. In this case, the spreading process is no longer axisymmetric, and a drop may bounce while sliding along inclined surfaces. Besides, gravity may help mitigate bouncing alongside solidification. These fields could find wide applications for numerical simulations.

Conflict of interest

None declared.

Acknowledgement

This research is supported by the Natural Science Foundation of the Jiangsu Higher Education Institutions of China (Grant No. 21KJB460034).

References

- [1]. Zhan, H., Lu, C., Liu, C., Wang, Z., Lv, C., & Qing, G. (2021). Horizontal motion of a superhydrophobic substrate affects the drop bouncing dynamics. *Physical Review Letters*, 126(23). <https://doi.org/10.1103/physrevlett.126.234503>
- [2]. Abouelsoud, M. (2021). Bouncing and coalescence dynamics during the impact of a falling drop with a sessile drop on different solid surfaces. *Physics of Fluids*, 33(6). 063309. <https://doi.org/10.1063/5.0050829>
- [3]. Wang, W., Chen, J., Lin, F., Zou, J., & Dorbolo, S. (2019). Water drops bouncing off vertically vibrating textured surfaces. *Journal of Fluid Mechanics*, 876, 1041–1051. <https://doi.org/10.1017/jfm.2019.576>
- [4]. Xiao, M., Liu, X., Zeng, S., Zheng, Z., Wang, G., Qiu, Z., Liu, M., & Zeng, D. (2021). Effects of particle size on the microstructure and mechanical properties of HVOF-Sprayed Al-Based quasicrystalline coatings. *Journal of Thermal Spray Technology*, 30(5), 1380–1392. <https://doi.org/10.1007/s11666-021-01202-1>
- [5]. Josserand, C., & Thoroddsen, S. T. (2016). Drop impact on a solid surface. *Annual Review of Fluid Mechanics*, 48(1), 365–391. <https://doi.org/10.1146/annurev-fluid->

[122414-034401](https://doi.org/10.1016/j.ijheatmasstransfer.2022.122710)

[6]. Liu, L., Zhang, Y., Cai, G., & Tsai, P. A. (2022). High-speed dynamics and temperature variation during drop impact on a heated surface. *International Journal of Heat and Mass Transfer*, 189, 122710.

<https://doi.org/10.1016/j.ijheatmasstransfer.2022.122710>

[7]. Han, X., Li, J., Tang, X., Li, W., Zhao, H., Yang, L., & Wang, L. (2022). Droplet Bouncing: fundamentals, regulations, and applications. *Small*, 18(22).

<https://doi.org/10.1002/sml.202200277>

[8]. Wang, H., Liu, C., Zhan, H., & Liu, Y. (2019). Droplet asymmetric bouncing on inclined superhydrophobic surfaces. *ACS Omega*, 4(7), 12238 – 12243.

<https://doi.org/10.1021/acsomega.9b01348>

[9]. Samkhaniani, N., Stroh, A., Holzinger, M. J., Marschall, H., Frohnäpfel, B., & Wörner, M. (2021). Bouncing drop impingement on heated hydrophobic surfaces. *International Journal of Heat and Mass Transfer*, 180, 121777.

<https://doi.org/10.1016/j.ijheatmasstransfer.2021.121777>

[10]. Sanjay, V., Chantelot, P., & Lohse, D. (2023). When does an impacting drop stop bouncing? *Journal of Fluid Mechanics*, 958, A26 <https://doi.org/10.1017/jfm.2023.55>

[11]. Kumar, A., & Pathak, M. (2023). Droplet impact on hydrophobic and superhydrophobic surfaces with the electrowetting technique. *Chemical Engineering Science*, 281, 119162. <https://doi.org/10.1016/j.ces.2023.119162>

[12]. Shen, M., Li, B. Q., Yang, Q., Bai, Y., Wang, Y., Zhu, S., Zhao, B., Li, T., & Hu, Y. (2019). A modified phase-field three-dimensional model for droplet impact with

solidification. *International Journal of Multiphase Flow*, 116, 51 – 66.

<https://doi.org/10.1016/j.ijmultiphaseflow.2019.04.004>

[13]. Wörner, M., Samkhaniani, N., Cai, X., Wu, Y., Majumdar, A., Marschall, H., Frohnappel, B., & Deutschmann, O. (2021). Spreading and rebound dynamics of sub-millimetre urea-water-solution droplets impinging on substrates of varying wettability.

Applied Mathematical Modelling, 95, 53–73.

<https://doi.org/10.1016/j.apm.2021.01.038>

[14]. Aziz, S. D., & Chandra, S. (2000). Impact, recoil and splashing of molten metal droplets. *International Journal of Heat and Mass Transfer*, 43(16), 2841 – 2857.

[https://doi.org/10.1016/s0017-9310\(99\)00350-6](https://doi.org/10.1016/s0017-9310(99)00350-6)

[15]. Liu, H. R., Ng, C. S., Chong, K. L., Lohse, D., & Verzicco, R. (2021). An efficient phase-field method for turbulent multiphase flows. *Journal of Computational Physics*,

446, 110659. <https://doi.org/10.1016/j.jcp.2021.110659>

[16]. Jha, A., Chantelot, P., Clanet, C., & Quéré, D. (2020). Viscous bouncing. *Soft*

Matter, 16(31), 7270–7273. <https://doi.org/10.1039/d0sm00955e>

[17]. Biance, A., Chevy, F., Clanet, C., Lagubeau, G., & Quéré, D. (2006). On the elasticity of an inertial liquid shock. *Journal of Fluid Mechanics*, 554(1), 47.

<https://doi.org/10.1017/s0022112006009189>

[18]. Liu, Q., Lo, J. H. Y., Li, Y., Liu, Y., Zhao, J., & Xu, L. (2021). The role of drop shape in impact and splash. *Nature Communications*, 12(1).

<https://doi.org/10.1038/s41467-021-23138-4>

[19]. Shen, M., Li, B. Q., & Bai, Y. (2020). Numerical investigation of solidification

microstructure formation in sequential YSZ droplet impact under supersonic plasma spraying. *International Journal of Heat and Mass Transfer*, 157, 119844.

<https://doi.org/10.1016/j.ijheatmasstransfer.2020.119844>